Pyrrhotites in asteroid 162173 Ryugu: Records of the initial changes on their surfaces with aqueous alteration

Hiroharu Yui, Shu-Hei Urashima, Morihiko Onose, Mayu Morita, Shintaro Komatani, Izumi Nakai, Yoshinari Abe, Yasuko Terada, Hisashi Homma, Kazuko Motomura, et al.

Geochimica et Cosmochimica Acta 379 (2024) 172–183

Contents lists available at ScienceDirect

Geochimica et Cosmochimica Acta

journal homepage: www.elsevier.com/locate/gca

Pyrrhotites in asteroid 162173 Ryugu: Records of the initial changes on their surfaces with aqueous alteration

Hiroharu Yui [a,*], Shu-hei Urashima [a], Morihiko Onose [b], Mayu Morita [b], Shintaro Komatani [b], Izumi Nakai [c], Yoshinari Abe [d], Yasuko Terada [e], Hisashi Homma [f], Kazuko Motomura [g], Kiyohiro Ichida [b], Tetsuya Yokoyama [h], Kazuhide Nagashima [i], Jérôme Aléon [j], Conel M. O'D. Alexander [k], Sachiko Amari [l,m], Yuri Amelin [n], Ken-ichi Bajo [o], Martin Bizzarro [p], Audrey Bouvier [q], Richard W. Carlson [k], Marc Chaussidon [r], Byeon-Gak Choi [s], Nicolas Dauphas [t], Andrew M. Davis [t], Wataru Fujiya [u], Ryota Fukai [v], Ikshu Gautam [h], Makiko K. Haba [h], Yuki Hibiya [w], Hiroshi Hidaka [x], Peter Hoppe [y], Gary R. Huss [i], Tsuyoshi Iizuka [z], Trevor R. Ireland [aa], Akira Ishikawa [h], Shoichi Itoh [ab], Noriyuki Kawasaki [o], Noriko T. Kita [ac], Kouki Kitajima [ac], Thorsten Kleine [ad], Sasha Krot [i], Ming-Chang Liu [ae], Yuki Masuda [h], Frédéric Moynier [r], Ann Nguyen [af], Larry Nittler [k], Andreas Pack [ag], Changkun Park [ah], Laurette Piani [ai], Liping Qin [aj], Tommaso Di Rocco [ag], Sara S. Russell [ak], Naoya Sakamoto [al], Maria Schönbächler [am], Lauren Tafla [ae], Haolan Tang [ae], Kentaro Terada [an], Tomohiro Usui [v], Sohei Wada [o], Meenakshi Wadhwa [ao], Richard J. Walker [ap], Katsuyuki Yamashita [aq], Qing-Zhu Yin [ar], Shigekazu Yoneda [as], Edward D. Young [ae], Ai-Cheng Zhang [at], Tomoki Nakamura [au], Hiroshi Naraoka [av], Takaaki Noguchi [aw], Ryuji Okazaki [av], Kanako Sakamoto [v], Hikaru Yabuta [ax], Masanao Abe [v], Akiko Miyazaki [v], Aiko Nakato [v], Masahiro Nishimura [v], Tatsuaki Okada [v], Toru Yada [v], Kasumi Yogata [v], Satoru Nakazawa [v], Takanao Saiki [v], Satoshi Tanaka [v], Fuyuto Terui [ay], Yuichi Tsuda [v], Sei-ichiro Watanabe [x], Makoto Yoshikawa [v], Shogo Tachibana [az], Hisayoshi Yurimoto [o]

[a] *Department of Chemistry, Tokyo University of Science, Tokyo 162-8601, Japan*
[b] *Analytical Technology, Horiba Techno Service Co., Ltd., Kyoto 601-8125, Japan*
[c] *Department of Applied Chemistry, Tokyo University of Science, Tokyo 162-8601, Japan*
[d] *Graduate School of Engineering Materials Science and Engineering, Tokyo Denki University, Tokyo 120-8551, Japan*
[e] *Spectroscopy and Imaging, Japan Synchrotron Radiation Research Institute, Hyogo 679-5198 Japan*
[f] *Osaka Application Laboratory, Rigaku Corporation, Osaka 569-1146, Japan*
[g] *Thermal Analysis Division, Rigaku Corporation, Tokyo 196-8666, Japan*
[h] *Department of Earth and Planetary Sciences, Tokyo Institute of Technology, Tokyo 152-8551, Japan*
[i] *Hawai'i Institute of Geophysics and Planetology, University of Hawai'i at Mānoa, Honolulu, HI 96822, USA*
[j] *Institut de Minéralogie, de Physique des Matériaux et de Cosmochimie, Sorbonne Université, Museum National d'Histoire Naturelle, Centre National de la Recherche Scientifique Unité Mixte de Recherche 7590, Institut de recherche pour le développement, Paris 75005, France*
[k] *Earth and Planets Laboratory, Carnegie Institution for Science, Washington, DC, 20015, USA*
[l] *McDonnell Center for the Space Sciences and Physics Department, Washington University, St. Louis, MO 63130, USA*
[m] *Geochemical Research Center, The University of Tokyo, Tokyo, 113-0033, Japan*
[n] *Guangzhou Institute of Geochemistry, Chinese Academy of Sciences, Guangzhou, GD 510640, China*
[o] *Department of Natural History Sciences, Hokkaido University, Sapporo 001-0021, Japan*
[p] *Centre for Star and Planet Formation, Globe Institute, University of Copenhagen, Copenhagen K 1350, Denmark*
[q] *Bayerisches Geoinstitut, Universität Bayreuth, Bayreuth 95447, Germany*
[r] *Université Paris Cité, Institut de physique du globe de Paris, Centre National de la Recherche Scientifique, Paris 75005, France*
[s] *Department of Earth Science Education, Seoul National University, Seoul 08826, Republic of Korea*
[t] *Department of the Geophysical Sciences and Enrico Fermi Institute, University of Chicago, Chicago, IL 60637, USA*
[u] *Faculty of Science, Ibaraki University, Mito 310-8512, Japan*

* Corresponding author.
E-mail address: yui@rs.tus.ac.jp (H. Yui).

https://doi.org/10.1016/j.gca.2024.06.016
Received 27 December 2023; Accepted 18 June 2024
Available online 23 June 2024

[v] Institute of Space and Astronautical Science (ISAS), Japan Aerospace Exploration Agency (JAXA), Sagamihara 252-5210, Japan
[w] Department of General Systems Studies, University of Tokyo, Tokyo 153-0041, Japan
[x] Department of Earth and Planetary Sciences, Nagoya University, Nagoya 464-8601, Japan
[y] Max Planck Institute for Chemistry, Mainz 55128, Germany
[z] Department of Earth and Planetary Science, University of Tokyo, Tokyo 113-0033, Japan
[aa] School of Earth and Environmental Sciences, University of Queensland, St Lucia, QLD 4072, Australia
[ab] Division of Earth and Planetary Sciences, Kyoto University, Kyoto 606-8502, Japan
[ac] Department of Geoscience, University of Wisconsin- Madison, Madison, WI 53706, USA
[ad] Max Planck Institute for Solar System Research, Göttingen 37077, Germany
[ae] Department of Earth, Planetary, and Space Sciences, University of California, Los Angeles, CA 90095, USA
[af] Astromaterials Research and Exploration Science Division, National Aeronautics and Space Administration Johnson Space Center, Johnson Space Center, Houston, TX 77058, USA
[ag] Faculty of Geosciences and Geography, University of Göttingen, Göttingen D-37077, Germany
[ah] Division of Earth-System Sciences, Korea Polar Research Institute, Incheon 21990, Korea
[ai] Centre de Recherches Pétrographiques et Géochimiques, Centre National de la Recherche Scientifique-Université de Lorraine, Nancy 54500, France
[aj] School of Science and Space Sciences, University of Science and Technology of China, Anhui 230026, China
[ak] Department of Earth Sciences, Natural History Museum, London SW7 5BD, UK
[al] Isotope Imaging Laboratory, Hokkaido University, Sapporo 001-0021, Japan
[am] Institute for Geochemistry and Petrology, Department of Earth Sciences, ETH Zurich, Zurich, Switzerland
[an] Department of Earth and Space Science, Osaka University, Osaka 560-0043, Japan
[ao] School of Earth and Space Exploration, Arizona State University, Tempe, AZ 85281, USA
[ap] Department of Geology, University of Maryland, College Park, MD 20742, USA
[aq] Graduate School of Natural Science and Technology, Okayama University, Okayama 700-8530, Japan
[ar] Department of Earth and Planetary Sciences, University of California, Davis, CA 95616, USA
[as] Department of Science and Engineering, National Museum of Nature and Science, Tsukuba 305-0005, Japan
[at] School of Earth Sciences and Engineering, Nanjing University, Nanjing 210023, China
[au] Department of Earth Science, Tohoku University, Sendai 980-8578, Japan
[av] Department of Earth and Planetary Sciences, Kyushu University, Fukuoka 819-0395, Japan
[aw] Division of Earth and Planetary Sciences, Kyoto University, Kyoto 606-8502, Japan
[ax] Earth and Planetary Systems Science Program, Hiroshima University, Higashi-Hiroshima 739-8526, Japan
[ay] Graduate School of Engineering, Kanagawa Institute of Technology, Atsugi 243-0292, Japan
[az] UTokyo Organization for Planetary and Space Science (UTOPS), University of Tokyo, Tokyo 113-0033, Japan

ARTICLE INFO

Associate editor: Martin Robert Lee

Keywords:
Ryugu
Pyrrhotite
Aqueous alteration
Magnetite

ABSTRACT

The surface chemistry of pyrrhotites from intact particles directly collected from asteroid (162173) Ryugu was investigated by micro-Raman spectroscopy. The Raman peak characteristic to pyrrhotite was observed at around 115 cm^{-1} in Ryugu pyrrhotites, similar to freshly cleaved surfaces of terrestrial pyrrhotites. Additional Raman bands centered at around 220, 275, and 313 cm^{-1} with broadened features were also detected from the Ryugu pyrrhotites. The set of Raman bands at 220 and 275 cm^{-1} was assigned to typical Fe-S stretching vibrations of ν_2 (225 cm^{-1}) and ν_1 (275 cm^{-1}). These bands are not clearly observed in bulk crystals of pyrrhotite but appear in its nanoparticulate phase. These bands are ordinarily seen in amorphous monosulfides that formed under low oxygen fugacity (fO_2) conditions in nature, indicating that the structural alteration of pyrrhotite surfaces occurred heterogeneously on the nanoscale under low fO_2 conditions. Further, the Raman band at 313 cm^{-1} was attributed to a characteristic tetrahedral bonding of Fe(III) in the lattice of $Fe^{II}_{1-3x}Fe^{III}_{1-2x}S$, followed by the local breakdown of the crystal lattice structures from planar bonding with Fe(II). In addition, some areas of the Ryugu pyrrhotite grains showed corroded structures with iridescence. Furthermore, assemblages of magnetite particles were also preferentially observed on small areas of the likely-dissolved pyrrhotite crystals in phyllosilicate matrices. These characteristic features in the Raman spectra and in corroded structures of Ryugu pyrrhotites record changes in the local environmental conditions via aqueous alteration. The corrosion of pyrrhotite crystals followed by the preferential formation of magnetite particles by asteroidal water is the likely product of dissolution of Fe(II) from the pyrrhotite surface and its oxidative precipitation in microchemical environments on the Ryugu parent body.

1. Introduction

Pyrrhotite is a common mineral found in iron sulfide ores and also in sulfidic and methanic sediments in nature (Roberts, 2015; Horng, 2018). It has a nonstoichiometric formula of $Fe_{1-x}S$ ($0 < x < 0.125$), permitting many superstructures. Two of the most common superstructures of pyrrhotite are monoclinic (Fe_7S_8) and hexagonal (Fe_9S_{10}) (Tang and Chen, 2022). The phase diagram of the stability of the iron sulfide system, including pyrrhotite, shows very complicated features that are dependent on thermodynamic conditions (Multani and Waters, 2018). In other words, the chemical states of pyrrhotites carry valuable information on the changes in aqueous environments where they formed and dissolved.

Micrometer-sized pyrrhotites were typically seen on the surfaces of the particles collected directly from asteroid (162173) Ryugu, indicating they occurred in aqueous environments on the parent body of Ryugu (Yokoyama et al., 2023; Nakamura et al., 2023). In fact, the initial analyses of Ryugu samples have revealed that they have similar mineralogical, petrological, and chemical features as the CI1 (Ivuna-type) carbonaceous chondrites, which experienced pervasive aqueous alteration (Yokoyama et al., 2023; Nakamura et al., 2023). Since pyrrhotites and related iron sulfides such as pentlandite and cubanite found in CI1 chondrites record the histories of the aqueous environments where they formed and altered (Bullock et al., 2005; Berger et al., 2016; Schrader et al., 2021), we expect that the investigation of the surface chemistries of the Ryugu pyrrhotites in detail should provide further important constraints on the thermodynamic and chemical conditions of aqueous environments on the parent body of Ryugu (Hopp et al., 2022; Kawasaki et al., 2022; Liu et al., 2022; Nakamura et al., 2022).

In the present study, we employed micro-Raman spectroscopy to investigate the surface chemistry of Ryugu pyrrhotites. The advantage of micro-Raman spectroscopy is that it does not require the careful surface

polishing generally required for quantitative analysis by electron-beam microscopy. Further, micro-Raman spectra are quite sensitive to the slight and local changes of the crystal structures. However, the application of the micro-Raman spectroscopy to the sulfides in meteorites has been quite limited. This is because the Raman scattering signals for pyrrhotite crystals are quite weak. In addition, the surfaces of iron sulfides are chemically sensitive and are readily oxidized by the abundant oxygen molecules (O_2) in the terrestrial atmosphere (Lara et al., 2015). In contrast, pyrrhotites in intact particles directly sampled from Ryugu are expected to be free from terrestrial alteration. Thus, Ryugu pyrrhotites should retain the original surface chemistry of iron sulfides that directly interacted with asteroidal water. As such, they can provide detailed information on the chemical and thermodynamic conditions of aqueous alteration that prevailed in the Ryugu parent body.

2. Materials and methods

2.1. Samples

Ryugu particles were extracted from their assemblage in the A0107 aggregate, which was collected during the first touchdown operation (Tachibana et al., 2022). Ryugu grains were categorized into four groups, namely, Dark (most dominant), Glossy, Bright, and White from the images taken by an optical microscope (Nakato et al., 2023). All of the particles investigated here had features consistent with the Dark group.

Terrestrial pyrrhotites sampled from Kavalerovo and Dalnegorsk (Primorsky Krai, Russia) were prepared for comparison with the Ryugu samples. However, outermost surfaces of the terrestrial pyrrhotites are heavily oxidized by the abundant O_2 in the terrestrial atmosphere. In contrast, the formation and alteration environments for Ryugu pyrrhotites likely occurred under much lower oxygen fugacity fO_2 conditions compared to the terrestrial atmosphere (Fujiya et al., 2023). Furthermore, the interior of the terrestrial sulfides were not necessarily in contact with the terrestrial atmosphere. Thus, the fresh surface of the interior of the terrestrial pyrrhotite should provide an important reference to study the chemical states of pyrrhotite surfaces under extremely low fO_2. To minimize terrestrial oxidation of pyrrhotite surfaces, we cleaved pyrrhotite from larger crystals with chisels just prior to the micro-Raman spectroscopic measurements. The freshly cleaved surfaces of terrestrial pyrrhotites with hexagonal morphologies are metallic silver in color. This is markedly different from general pyrrhotite surfaces that have been exposed for a long time under terrestrial atmosphere, which have a yellowish luster. It is also worth noting that the spectroscopic features of the freshly-cleaved pyrrhotite surfaces change in the timescale of a few days under terrestrial atmosphere. Thus, the freshly-cleaved fragments of terrestrial pyrrhotites with chisels under atmospheric condition were quickly transferred into N_2 gas-purged vial containers within a minute for the following Raman spectroscopic measurements. The Raman spectra of fresh surfaces of terrestrial pyrrhotite fragments were measured just after the cleavage of the sample and in a N_2-gas-purged chamber. The details of this are described in Urashima et al. (2022).

2.2. Instruments

Micro-Raman spectroscopic observation of Ryugu particles was performed using a LabRAM HR Evolution equipped with a grating (300 grooves/mm) and a Synapse EMCCD detector (HORIBA Co., Ltd.). The confocal optical arrangement of the reflected light microscope and autofocusing stage-driving with the LabSpec 6 software (HORIBA Co., Ltd.) enabled us to obtain Raman spectra of sample minerals with surface roughness and micro-meter-sized porous structures without any pretreatment, such as surface polishing. An Olympus LMPlanFN (x100, NA 0.80, WD 3.4 mm) was used as an objective lens for efficient collection of the weak Raman signal from the pyrrhotites. The excitation wavelength was fixed at 532 nm, and the laser power was adjusted to be 0.6 mW for pyrrhotite observation to prevent damage by laser heating. The duration for the signal accumulation of the Raman signal was limited to 120 s at the same focal spot of the laser beam to avoid excess heating of the spot area. N_2 gas was circulated in the sample chamber to minimize oxidization of the pyrrhotite surfaces during the measurements. The handling of the Ryugu particles in the optical cells for the Raman spectroscopic measurements was also carried out in a N_2 gas-purged chamber. Thus, the exposure of Ryugu pyrrhotite grains to the vapor and oxygen-rich laboratory atmosphere was kept as minimum as possible.

The custom-made micro-Raman instrument was also used for the measurements of terrestrial pyrrhotites, especially for the measurements in the lower wavenumber region, was also used for the measurements of terrestrial pyrrhotites. The details of this are described in Urashima et al. (2022).

For spectral data processing, raw data were recorded by the LabSpec 6 software (HORIBA Co., Ltd.). The averaging and graphical visualization of the spectral raw data were performed with the Igor pro 8 software (WaveMetrics). We showed the spectral data without subtracting background in the manuscript. This is because the background signals (i.e. strong Rayleigh wing scattering from the metallic surface of pyrrhotites, fluorescence from phyllosilicate matrix, and so on) have also information on the local sample heterogeneity. We discerned the Raman signals from pyrrhotite surfaces by comparing these overwrapping background signals.

3. Results

3.1. Thermal damage test for Ryugu pyrrhotites under laser irradiation

Since the surface of pyrrhotite is sensitive to heating, it is important to be careful while performing micro-Raman spectroscopic observations on pyrrhotite (Urashima et al., 2022). Even under less oxidizing environments, thermal damage of the pyrrhotite surface may occur within a few seconds from excess irradiation of the laser beam. Especially, in micro-Raman spectroscopic measurements, a laser beam is focused on the sample surface via an objective lens, and the irradiation area is locally but extensively heated. If oxygen molecules are present, pyrrhotites readily transform to hematite (Fe_2O_3) owing to the acceleration of the oxidation by laser heating (Xi et al., 2019). Therefore, we first investigated the appropriate power and duration of laser irradiation for the measurements of the Ryugu pyrrhotites.

Fig. 1 (a) and (b) show typical reflected light images of Ryugu pyrrhotite before and after the laser irradiation of 3.0 mW under circulating N_2 gas. Even under the oxygen-free conditions, we found that the metallic luster of the original pyrrhotite surface was lost by thermal damage due to the 3.0-mW laser irradiation. Fig. 1 (c) shows the temporal change of the Raman spectra with the 3.0-mW laser irradiation. Two intense and sharp Raman peaks appeared just after the laser irradiation on the surface. Taking into account the absence of other intense and sharp Raman peaks, the two peaks were identified as marcasite (FeS_2, 323 cm^{-1} and 388 cm^{-1} for a single crystal), another thermally stable phase of iron sulfide under atmospheric pressure (Lutz and Müller, 1991). Since the energy of the laser spot has a Gaussian distribution, the focused area of the laser beam should have a local but a steep temperature gradient. Thus, we can consider that the pyrrhotite surface partially melted and transformed into marcasite at the center spot of the irradiation area of the focused laser beam. However, owing to O_2-free conditions because of the N_2 gas circulation in the sample chamber, the pyrrhotites did not transform to hematite from a reaction with oxygen molecules.

By lowering the power of the excitation laser beam, we found that the irradiation power of 0.6 mW was the most appropriate for the measurements of Ryugu pyrrhotites under our instrumental setup. Fig. 2 shows the irradiation test for Ryugu pyrrhotite at a laser power of 0.6

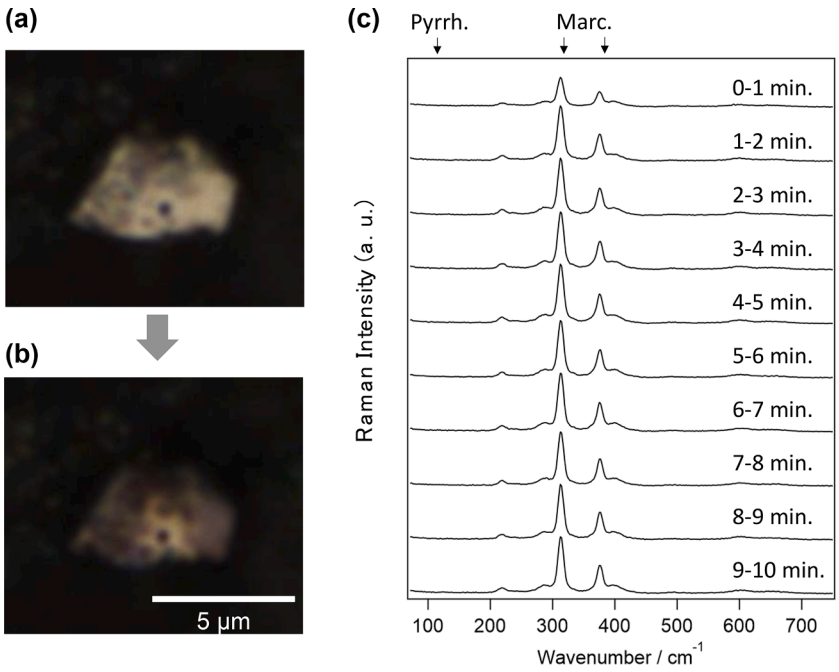

Fig. 1. Thermal damage test of laser irradiation on Ryugu pyrrhotite for obtaining appropriate conditions of laser power and irradiation duration. (a) and (b) Reflected light images of before and after laser irradiation. (c) Temporal changes in the spectra. Even in the Raman spectrum measured in the first minute of laser irradiation, pyrrhotite had transformed into another iron sulfide phase similar to marcasite, characterized by the Raman peaks of in-phase stretching modes (A_g symmetry) appeared at around 320 and 385 cm^{-1}, by thermal annealing. The peak positions of a single crystal of marcasite (323 cm^{-1} and 388 cm^{-1}) reported by Lutz and Müller (1991) are indicated as arrows. The representative peak position of pyrrhotite (115 cm^{-1}) reported by Urashima et al. (2022) is also shown.

mW. The characteristic peak for pyrrhotite was observed at around 115 cm^{-1} (Urashima et al., 2022), indicating its crystal structure was unaffected during the 10-minute irradiation. The spectra in Fig. 2 lack peaks that are characteristic of iron oxides and (oxy)hydroxides, which are typically intense and occur in the range 350–750 cm^{-1} for terrestrial pyrrhotites exposed to the O_2-rich terrestrial atmosphere (de Faria et al., 1997; Hanesch, 2008; Urashima et al., 2022). No other significant changes in Raman spectra were detected, but three minor, broad bands appeared in the range of 200–350 cm^{-1}, whose assignments will be discussed below. Based on these results for the measurements of Ryugu pyrrhotites surfaces under our instrumental setup, we limited the duration of signal accumulation with the 0.6-mW laser power to 2 min (120 s) at the same spatial spot.

3.2. Comparisons of the Raman spectra of Ryugu and terrestrial pyrrhotites

To compare the similarities and the differences between Ryugu and terrestrial pyrrhotites, we first measured the Raman spectra of terrestrial pyrrhotites. Without any cleaving and polishing pre-treatment of the surfaces of terrestrial pyrrhotites, they were a somewhat yellow hue with a metallic luster. Fig. 3 (a) shows the Raman spectrum of an intact surface of a terrestrial pyrrhotite from Kavalerovo. We observed many Raman peaks from iron oxides formed on the pyrrhotite surface, such as hematite (the most intense peak at around 1300 cm^{-1}) and magnetite (at 660–680 cm^{-1}) (de Faria et al., 1997; Hanesch, 2009). As mentioned above, since the pyrrhotite surface is highly reactive, its oxidative corrosion to magnetite and hematite readily occurs in the O_2-rich terrestrial atmosphere. Fig. 3 (b) shows the fresh surface of the terrestrial pyrrhotite from Kavalerovo prepared by cleaving just before the Raman spectroscopic measurements. The Raman peaks from iron oxides were no longer present in the cleaved samples. The color of the surface was gray in hue with a metallic luster. In addition, the same experiments were performed on another terrestrial pyrrhotite sampled from Dalnegorsk, and the results are shown in Fig. 3 (c) and (d). As observed for the Kavalerovo pyrrhotite (Fig. 3 (a) and (b)), iron oxide peaks were observed on the uncleaved surface, while they were absent from the fresh surface.

Fig. 3 (e)–(h) compares Ryugu pyrrhotites and terrestrial ones in the lower wavenumber region (70–400 cm^{-1}). The characteristic peak for pyrrhotite appears at around 115 cm^{-1} (Urashima et al. 2022), and was observed for both Ryugu and terrestrial pyrrhotites. One notable characteristic was the appearance of three bands in the ranges of 200–350 cm^{-1} for the Ryugu pyrrhotites. The assignments of these Raman bands will be discussed in the section 4.1.

3.3. Typical Raman spectra of Ryugu pyrrhotites with hexagonal and lath morphologies

The morphologies of the Ryugu pyrrhotites are roughly categorized into two types: hexagonal and lath. These shapes are common for pyrrhotite and related iron sulfides found in both CI1 chondrites and Ryugu grains (Bullock et al., 2005; Alfing et al., 2019; Nakato et al., 2023; Yokoyama et al., 2023; Nakamura et al., 2023). The differences in the shapes of the pyrrhotites may be related to their superstructures (Tang and Chen, 2022). Another possible explanation for the differences in the shapes of the pyrrhotites is that the grains are simply viewed down different orientations. The hexagonal morphology would be viewing the pyrrhotite down the *c* axis, whereas the lath morphology would be viewing the pyrrhotite from the side (*a* or *b* axes). In either case, Raman spectroscopic comparisons of pyrrhotites between hexagonal and lath morphologies can provide information on the differences in their surface crystal structures and resultant stabilities and/or chemical reactivity during aqueous alteration.

Fig. 4 compares the typical Raman spectra of Ryugu pyrrhotites with hexagonal and lath shapes without any background correction. In both morphologies, the characteristic Raman peak for pyrrhotite appears at around 115 cm^{-1}. Furthermore, three characteristic Raman bands ranging from 200–350 cm^{-1} were also observed in both hexagonal and lath morphologies. Several Ryugu pyrrhotites were observed in this

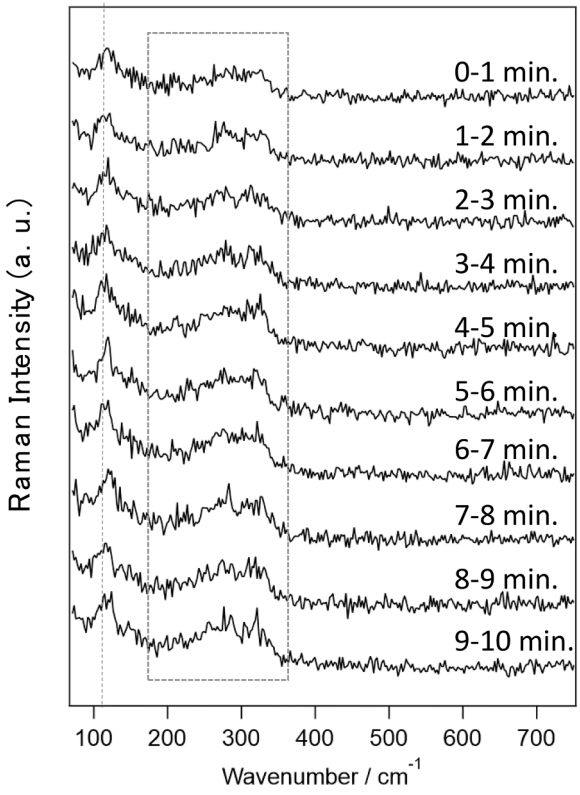

Fig. 2. Laser irradiation test for Ryugu pyrrhotite with 0.6 mW excitation. The characteristic Raman peak for pyrrhotite at around 115 cm^{-1} (indicated as dashed line) was observed. Additional Raman bands ranging 200–350 cm^{-1} (indicated as dashed square) were also discerned from background from the beginning of laser irradiation. The spectral features of the Raman peak (at 115 cm^{-1}) and bands (within 200–350 cm^{-1}) did not change during the measurements (10 min) with 0.6 mW excitation.

study, and almost all the Ryugu pyrrhotites showed these characteristic Raman bands. We also note that Raman peaks characteristic to iron oxides or (oxy)hydroxides in the range of 350–750 cm^{-1} were not observed for the Ryugu pyrrhotites, indicating their formation and alteration environments were under low fO_2. This will be discussed in the section 4.2.

Fig. 5 shows the peak positions of the averaged Raman spectra of Ryugu pyrrhotites with hexagonal and lath morphologies. The intensity ratios of the three bands ranging from 200–350 cm^{-1} were somewhat different for each grain. Another difference is the appearance of a peak at 85–90 cm^{-1} for hexagonal pyrrhotite. The details of these spectroscopic features and their relation to their surface structures with aqueous alteration will be discussed in the section 4.3.

3.4. *Comparisons of the corrosion features on both hexagonal and lath morphologies of Ryugu pyrrhotites*

Using reflected light microscopy, we found that some Ryugu pyrrhotites with corroded features showed iridescence, especially on the basal plane of the hexagonal pyrrhotite. Fig. 6 shows an example of the reflected light images of Ryugu pyrrhotite with hexagonal morphology. Note the iridescence on some areas of the surface and at the rims of the pyrrhotite grain. Furthermore, there are many small patches with iridescence and also isolated particles in and around the pyrrhotite grain. Since the iridescence of metal surfaces can often be related to the formation of thin metal oxides by surface corrosion (Martinez et al. 2007; Xue et al. 2011; Parkinson 2016; Lin et al. 2018; Cong et al., 2020), it is expected that these corroded features retain important records on the initial change of the surface structures induced by aqueous alteration.

Fig. 7 also shows the reflected light images of the corroded feature on the surface of Ryugu pyrrhotite grains with a lath morphology. Similar surface structures to the hexagonal grains, with iridescence and the scattered particles at the rims, were also observed. The shape of the corroded area on the grain seems to change from linear features to multiple patches. The linear features show iridescence, whereas the patches do not.

In primitive carbonaceous chondrites, the secondary formation of magnetite (Fe_3O_4) from primary iron sulfides has been observed and attributed to oxidation during aqueous alteration (Choi et al. 1997; Choi et al., 2000; Choi and Wasson, 2003; Davidson et al. 2014; Jilly-Rehak et al. 2018; Singerling and Brearley 2020). Thus, these changes in the surface structure and color of pyrrhotites found in intact Ryugu particles (Figs. 6 and 7) may record the extent of the initial reaction induced by aqueous alteration that occurred on the Ryugu parent body.

Fig. 8 (a) shows a reflected light image of the area after partially and likely dissolved Ryugu pyrrhotite with a hexagonal morphology. Fragments of the pyrrhotite with iridescence are scattered in the area. Fig. 8 (b) shows the examples of the Raman spectra of the fragments (A–D indicated in Fig. 8(a)) measured at this area. Fig. 9 (a) shows the assemblages of white particles in the areas after partially and likely dissolved Ryugu pyrrhotites with a hexagonal morphology. We measured Raman spectra of the particles (A–D indicated in Fig. 9 (a)) in these areas. Typical examples are shown in Fig. 9 (b), and the characteristic bands were assigned to magnetite. The chemical reactions involving pyrrhotite altering to magnetite and the corresponding chemical and thermodynamic conditions are discussed in the following sections.

4. Discussion

4.1. *Assignment of the characteristic Raman bands observed from the surface of Ryugu pyrrhotites*

Firstly, it should be noted that Raman signals from pyrrhotites are quite weak and often have strong backgrounds. The background with a negative slope (<350 cm^{-1}) observed in the Raman spectra in Fig. 4 is due to Rayleigh wing scattering from the strong reflection by metallic surfaces. In addition, a background with a positive slope (>350 cm^{-1}) is sometimes observed due to the strong fluorescence from the phyllosilicate matrices of the Ryugu particles. This occurs when the focusing area of the laser beam is within a few microns of the matrix material.

Secondly, we should be aware of oxidative corrosion by oxygen molecules and water vapor that is often observed in iron sulfides on meteorite surfaces exposed to the terrestrial atmosphere. This oxidative corrosion often results in the occurrence of iron oxides and (oxy)hydroxides showing characteristic intense Raman peaks mainly in the range of 350–750 cm^{-1}. For examples, magnetite shows three bands (310 cm^{-1}, 540 cm^{-1}, and 670 cm^{-1}) bands, maghemite also has three bands (350 cm^{-1}, 500 cm^{-1}, and 700 cm^{-1}), natural two-line ferrihydrite shows only the strong band (710 cm^{-1}), and synthetic six-line ferrihydrite has three bands (370 cm^{-1}, 510 cm^{-1}, and 710 cm^{-1}) (de Faia et al. 1997; Mazzetti and Thistlethwaite 2002; Hanesch 2009). These Raman peaks of iron oxides and (oxy)hydroxides were not detected in Ryugu pyrrhotites, owing to the freshness of the intact samples which were directly returned from the asteroid (Fig. 4).

Thirdly, before starting the discussion of the spectral features at 200–350 cm^{-1}, we should also be aware of the contribution from other iron sulfide phases, namely pentlandite $(Fe, Ni)_9S_8$ and cubanite $CuFe_2S_3$. This is because these sulfides are also found in Ryugu (Yokoyama et al., 2023; Nakamura et al., 2023) as well as other heavily aqueously altered samples, such as CI1 chondrites and samples from comet 81P/Wild 2 (Macdougall and Kerridge, 1977; Bullock et al., 2005; Berger et al., 2011; Berger et al., 2016). Ryugu samples were reported to show strong similarities to both CI1 chondrites and stardust samples from comet 81P/Wild 2 (Kawasaki et al., 2022). Pentlandite and

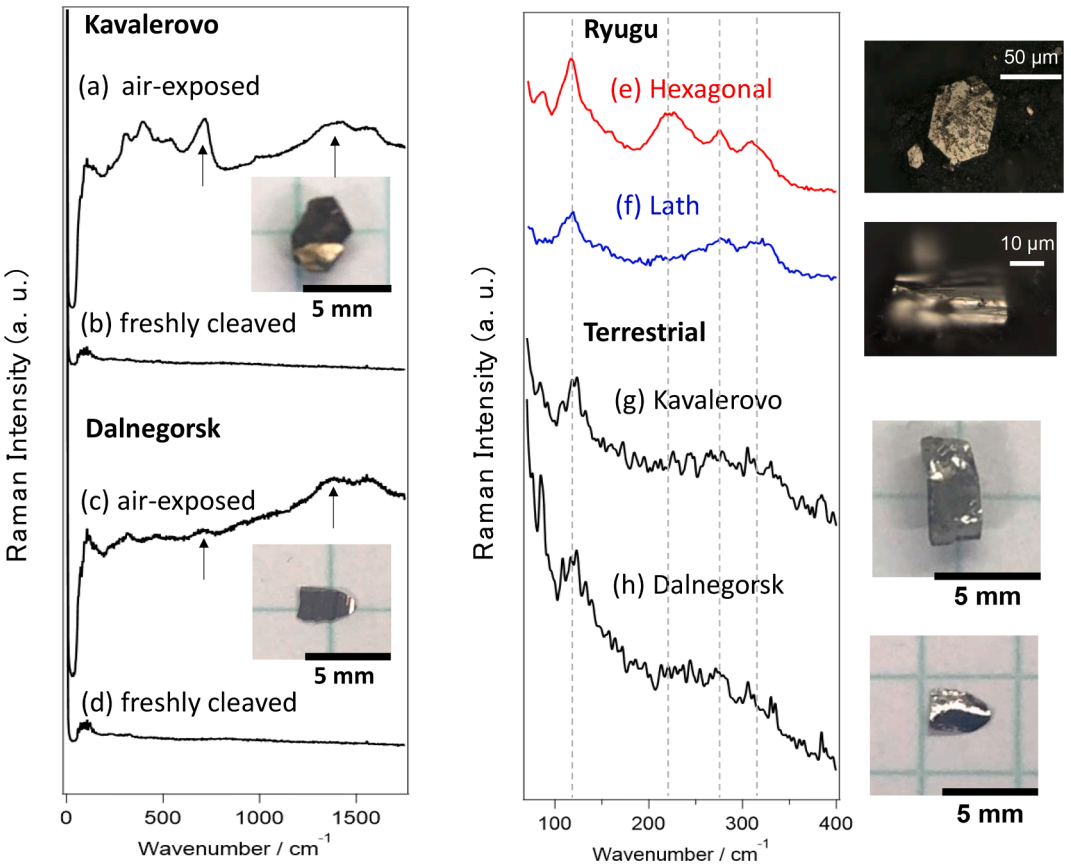

Fig. 3. Comparison of the Raman spectra of terrestrial and Ryugu pyrrhotites. (a) – (d): Comparisons of the Raman spectra of terrestrial pyrrhotites before and after cleaving ((a) and (b) Kavalerobo; (c) and (d) Dalnegorsk). Black arrows indicate the representative peak positions for magnetite (at 660 – 680 cm^{-1}) and hematite (at around 1300 cm^{-1}). (e) – (h): Comparisons of the Raman spectra of Ryugu pyrrhotites with (e) hexagonal and (f) lath shape in the lower wavenumber region and with the cleaved fresh surfaces of terrestrial pyrrhotites from (g) Kavalerovo and (h) Dalnegorsk. The dashed line indicates the representative peak position of pyrrhotite (at 115 cm^{-1}). The dashed lines show the wavenumbers of the characteristic set of Raman bands observed within a range of 200 to 350 cm^{-1}, that were clearly discerned from the background of the spectrum for Ryugu pyrrhotite with hexagonal shape.

cubanite show intense and characteristic sets of two Raman peaks above 300 cm^{-1} (pentlandite: 323 and 380 cm^{-1}; cubanite: 337 and 376 cm^{-1}) (Mikuła et al., 2021; Pankrushina et al., 2023). However, the surfaces of pyrrhotite crystals investigated in the present study did not show these peaks in their Raman spectra.

Based on these spectral confirmations, the assignments of the main Raman peak centered at around 115 cm^{-1} and the additional three bands centered at 225, 275, and 313 cm^{-1} are discussed by comparing them with terrestrial pyrrhotites. In the Raman spectra of air-exposed terrestrial pyrrhotites (Fig. 4 (a) Kavalerovo and (c) Dalnegorsk), Raman peaks of oxides (mainly hematite and magnetite) dominate the spectra (as indicated with arrows). In contrast, none of these peaks were visible when we observed the freshly cleaved surfaces (Fig. 4 (b) and (d)). In the Fig. 4 (e)–(f), the main peak at 115 cm^{-1}, which is characteristic of the pyrrhotite crystal structure, was always observed in the Raman spectra of Ryugu pyrrhotites with both hexagonal and lath morphologies. Additional Raman bands at 225, 275, and 313 cm^{-1} in Ryugu pyrrhotites that are not apparent in terrestrial pyrrhotites. Further, the bandwidths of these Raman bands have broadened features, indicating that they reflect some inhomogeneity in the local crystal structures on the pyrrhotite surfaces. The relation between these Raman bands and the surface structures of Ryugu pyrrhotites will be discussed in the following section from the viewpoint of aqueous alteration.

4.2. Local amorphous structures found on the surfaces of Ryugu pyrrhotites

To assign the three bands centered at around 225, 275, and 313 cm^{-1} in the Ryugu pyrrhotites, we compared them with artificial pyrrhotites synthesized under chemically and thermodynamically controlled conditions. The reason for choosing artificial pyrrhotites for the assignment is that they are purely and uniformly synthesized with controlled compositions and structures and can be well characterized. For the iron monosulfide (FeS) system, pyrrhotite, troilite, and mackinawite have been extensively studied from the viewpoint of nanomaterial synthesis and surface corrosion chemistry (Hansson et al., 2006; El Mendili et al., 2013; Genchev and Erbe, 2016; Matamoros-Veloza et al., 2018; Zhou et al., 2019), allowing the set of broadened Raman bands centered at around 225 cm^{-1} and 275 cm^{-1} to be assigned to Fe-S stretching modes with ν_2 (225 cm^{-1}) and ν_1 (275 cm^{-1}) of the nanoparticulate phase (Matamoros-Veloza et al., 2018). Since the nanoparticulate phase has various surfaces and edges that are distinct from the bulk phase, the crystal symmetry in the infinite lattice structure of the pyrrhotite bulk phase is expected to be effectively broken. This should result in the activation of the Fe-S stretching Raman modes that are inherently inactive in the infinite crystalline phases. Broadening of the Fe-S stretching Raman bands suggests they are derived not from a homogeneous structure but from the lattice structures with inhomogeneity. It is also worth mentioning that the set of two characteristic Raman bands centered at around 225 and 275 cm^{-1} are observed not only in artificial nanoparticulate iron monosulfides, but in natural amorphous

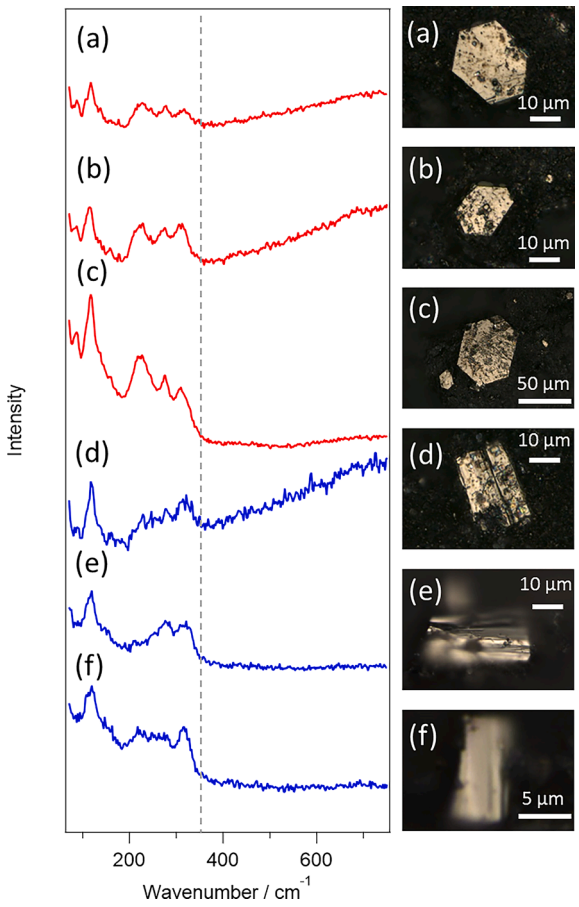

Fig. 4. Comparison of several Raman spectra of Ryugu pyrrhotites with (a)-(c) hexagonal shape and (d)-(f) lath shapes with corresponding images observed by reflected light microscope. The laser irradiation power was 0.6 mW, and data accumulation duration was 120 s at each spot. The spectra were measured at > 10 different spots in each grain, and they were averaged to improve signal-to-noise ratio. Because peak intensity for each raw spectrum was comparable to each other, no pretreatment such as intensity normalization was performed for the average. The characteristic Raman peak for pyrrhotite was detected at 115 cm^{-1} for all of the spectra (a)-(f). An additional three Raman bands at 225, 275, and 313 cm^{-1} were also discerned from the background, especially for the pyrrhotites with a hexagonal morphology. The dashed line indicates the spectral position of Raman shift at 350 cm^{-1}, for distinguishing other Raman peaks of iron oxides and (oxy)hydroxides that generally have intense peaks above 350 cm^{-1}. No peak from iron oxides and (oxy)hydroxides was observed. A background with a positive slope (>350 cm^{-1}) was sometimes observed due to the strong fluorescence from the phyllosilicate matrices of Ryugu particles when the focusing area of the laser beam included matrices simultaneously at the edges or corroded areas of the pyrrhotite grain.

pyrrhotites found in sediments formed under low fO_2 environments (Boughriet et al., 1997). In the sediments formed under low fO_2 conditions, pyrrhotite can be free from extensive oxidization by the direct attack of oxygen molecules. When pyrrhotites are exposed to an O_2-rich atmosphere, the surface of pyrrhotite grains should readily change to more thermodynamically stable phases, such as hematite. The oxidation to hematite is ubiquitously observed on pyrrhotite surfaces exposed to the terrestrial atmosphere. Hematite shows many intense Raman peaks, and these peaks readily surpass the intensities of the set of Raman bands (225 and 275 cm^{-1}) that are inherently weak. Thus, the disappearance of the strong peaks corresponding to iron oxides and the appearance of the set of Raman bands at around 225 and 275 cm^{-1} on Ryugu pyrrhotite surfaces show that the Ryugu pyrrhotites are free from terrestrial alteration, and that the surface alteration of Ryugu pyrrhotites occurred in low fO_2 environments. This is in good accordance with the model calculations for the chemical thermodynamic conditions of aqueous alteration that occurred on the parent bodies of carbonaceous chondrites (Zolensky et al., 1989; Singerling and Brearley 2020). For an example, the value of log fO_2 was suggested to be less than the hematite stability field (Singerling and Brearley 2020). Further, the appearance of the set of Raman bands at around 225 and 275 cm^{-1} is expected to record nanoscale structural changes on pyrrhotite surfaces by aqueous alteration in its initial stages.

The band centered at around 313 cm^{-1} is typically observed in the local tetrahedral lattice structure of Fe(III) formed in the FeS system (Robineau et al., 2017; Baum et al., 2018). Therefore, the corresponding chemical formula for the pyrrhotite system is noted as $Fe^{II}_{1-3x}Fe^{III}_{2x}S$. Since Fe(III) favors tetrahedral bonding with surrounding S(−II)s, disordering of the local crystal structure around Fe(III) should occur. This is also in good agreement with the occurrences of the local inhomogeneous structure of the pyrrhotite surfaces that are represented by the appearance of characteristic Raman bands of Fe-S stretching modes (225 cm^{-1} and 275 cm^{-1}). These inhomogeneities are typically observed in the nanoparticulate phases in FeS systems, rather than the infinite crystal structure.

The assignment of the Raman peak at 85–90 cm^{-1} for hexagonal pyrrhotites should also be mentioned. The origin of the peak is not yet clear. This is because the low-frequency region (<100 cm^{-1}) of the Raman spectrum of pyrrhotite and related iron monosulfide has not been fully elucidated (Urashima et al. 2022). One characteristic peak at 85 cm^{-1} was hardly seen in the pyrrhotite with lath morphology. This feature suggests the peak at 85 cm^{-1} reflects the difference in the orientation of the lattice structure and in the facets of pyrrhotite crystals (Multani and Waters, 2018).

4.3. Possibilities of the dissolution of pyrrhotite and following precipitation of magnetite under aqueous alteration

Finally, we discuss the physical and chemical features of the corroded parts of Ryugu pyrrhotites as observed by reflected light microscopy. Nakato et al. (2023) reported smooth, stepped, and altered textures on the surfaces of Ryugu pyrrhotites by FE-SEM-EDS. They suggested that space weathering is a possible origin for the altered texture. In the present observation by reflected light microscopy under visible (white) illumination, the iridescence was generally observed at such corroded surface textures (Figs. 6 and 7). The texture gradually transforms from a linear shape to aligned multiple but separated patches and then finally disappears (Fig. 6 (b) and (c), Fig. 7 (b) and (c)). Such gradual changes recorded on the surface structure of the corroded areas can provide information on the local environmental changes by aqueous alteration.

Further corroded features of pyrrhotite crystals are shown in Fig. 8. Fragments of pyrrhotite and particles with a yellow hue and an iridescence are scattered in the matrix area where pyrrhotite with hexagonal morphology likely dissolved (Fig. 8 (a)). Fig. 8 (b) shows examples of Raman spectra observed from the particles (A-D) in this area. Under the terrestrial atmosphere, where oxygen and vapor water molecules are abundant, (oxy)hydroxides are typical intermediate phases during the formation of iron oxides. In addition, thin films of (oxy)hydroxides and iron oxides formed on corroded iron surfaces textures generally show iridescence (Martinez et al. 2007; Xue et al. 2011; Parkinson 2016; Lin et al. 2018; Cong et al. 2020). These (oxy)hydroxides and iron oxides exhibit intense Raman peaks at around 600–750 cm^{-1} (Boughriet et al., 1997). However, Raman peaks from (oxy)hydroxides and iron oxides were not observed from particles A-D, indicating the corrosion of the Ryugu pyrrhotite differs from that which occurs on terrestrial pyrrhotites in an O_2-rich atmosphere.

Another possible pathway for the corrosion of Ryugu pyrrhotites is dissolution with their cathodic decomposition. Such cathodic decomposition of pyrrhotite was reported in deoxygenated solutions at the temperature of 25 ℃, a near-neutral pH (6.8) and an electrical potential

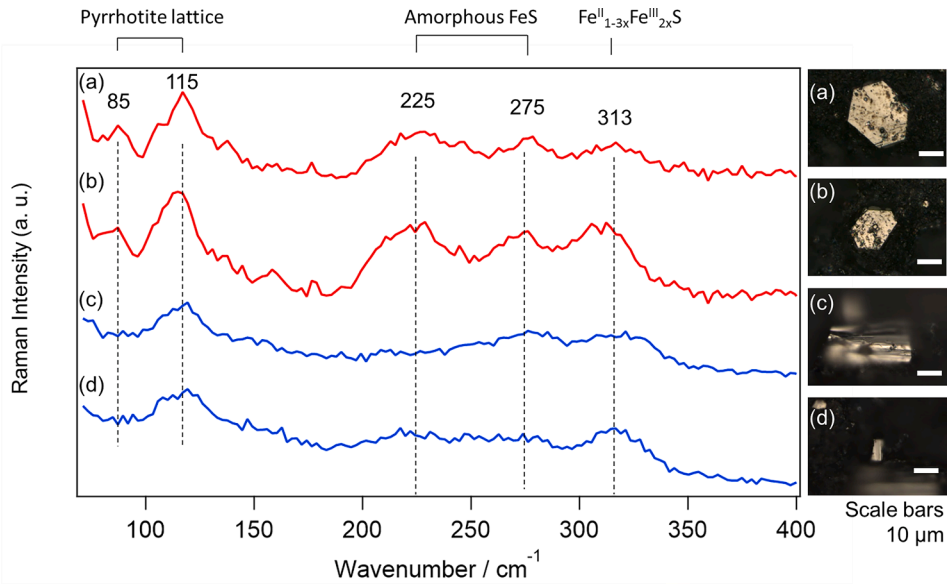

Fig. 5. Comparison of the averaged Raman peaks for pyrrhotites between with hexagonal plate structure ((a) and (b)) and with lath-shaped structure ((c) and (d)). The set of Raman bands at 225 cm^{-1} and 275 cm^{-1} are consistent with the Fe-S stretching modes of amorphous pyrrhotite, and the band at ~ 313 cm^{-1} is consistent with the local tetrahedral lattices of Fe(III) formed on the pyrrhotite surface, denoted as $Fe^{II}_{1-3x}Fe^{III}_{2x}S$.

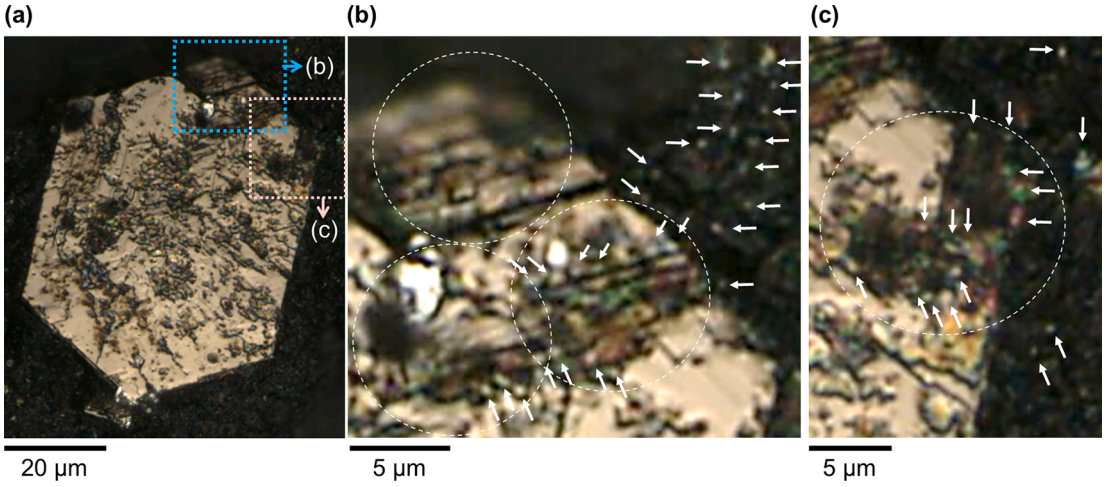

Fig. 6. Reflected light images of the corroded regions on the surface of Ryugu pyrrhotite (indicated as dashed-circles); (a) An example of the overall Ryugu pyrrhotite with hexagonal morphology. (b) and (c) Enlarged images of corroded parts with iridescence. White arrows indicate the positions of patches and scattered particles.

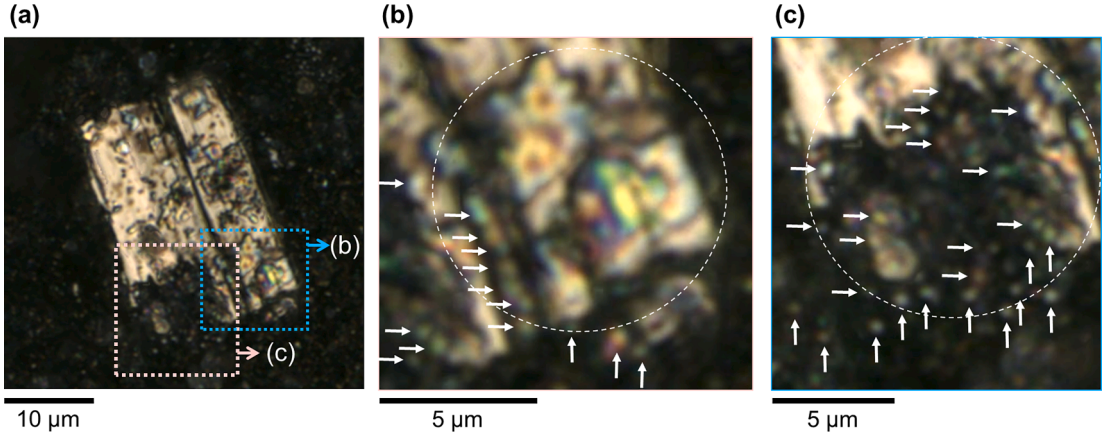

Fig. 7. Reflected light images of the corroded regions on the surface of Ryugu pyrrhotite (indicated as dashed-circles); (a) An example of the overall Ryugu pyrrhotite with lath structure. (b) and (c) Enlarged images of corroded parts with iridescence. White arrows indicate the positions of patches and scattered particles.

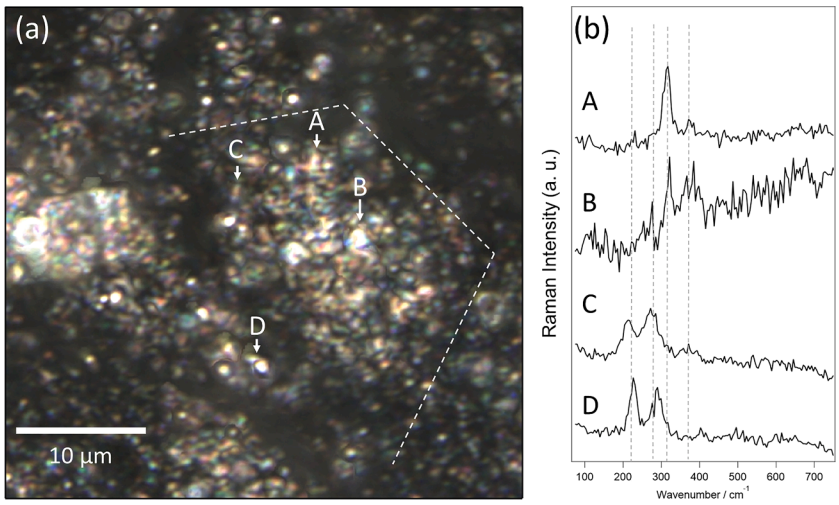

Fig. 8. (a) Reflected light image of the area of highly and likely dissolved Ryugu pyrrhotites with hexagonal and lath morphologies. Dashed lines show the edges of the original pyrrhotite with a hexagonal morphology for the aid of visibility. (b) Examples of Raman spectra of small fragments measured in the area. The corresponding location to each spectrum (A-D) is indicated with white arrow in the Fig. 8 (a). Four dashed lines in the Fig. 8(b) indicate the peak positions of 225, 275, 320, and 380 cm^{-1}. (A and B) Raman bands observed at around 320 cm^{-1} and 380 cm^{-1} are characteristic of pentlandite. (C and D) Raman bands observed at around 225 cm^{-1} and 275 cm^{-1} are assigned to Fe-S stretching mode particulate (amorphous) pyrrhotites. The decrease in the Raman shift and broadened bandwidth of these bands can be explained by the relative decrease in the crystallinity. In the present case, the fragment C is more amorphous than the fragment D.

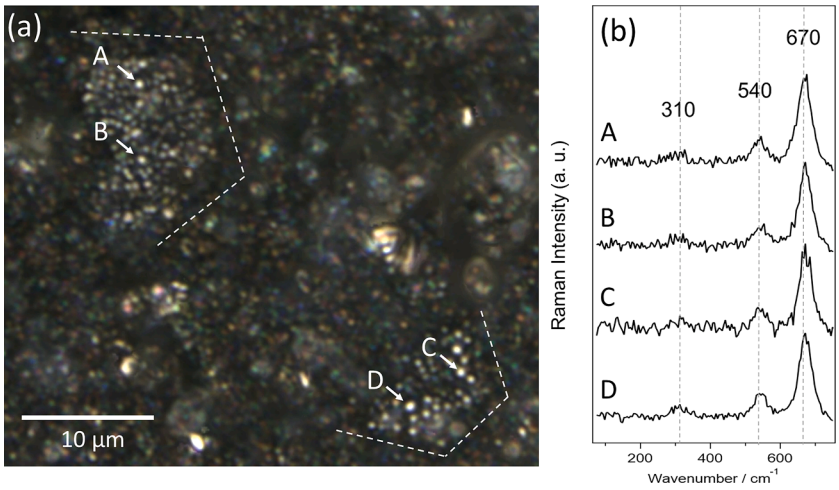

Fig. 9. (a) Reflected light image of the areas of altered Ryugu pyrrhotites with a hexagonal morphology. Dashed lines show the edges of the areas after pyrrhotites with a hexagonal morphology for the aid of visibility. (b) Typical Raman spectra of the particles (A-D) in their assemblage on the areas. The corresponding areas to each spectrum (A-D) are indicated with white arrows in the Fig. 9 (a). Three dashed lines in the Fig. 9(b) indicate the peak positions of 310, 540, and 670 cm^{-1}. All show characteristic Raman peaks for magnetite (310, 540, and 670 cm^{-1}).

(Eh) of −0.455 V (Cheng et al. 1998). An example of the carhodic decomposition pyrrhotite (Fe_7S_8) is shown as follows.

$$Fe_7S_8\ (s) + 2H^+ + 2e^- \rightarrow 6FeS + Fe^{2+} + 2HS^- \quad (1)$$

It is worth noting that the solution conditions (deoxygenated, temperature, pH, and Eh) are close to those expected for model calculations based on the interaction with the initial mineralogy for CI-type rocks (Zolensky et al., 1989; Rosenberg et al. 2001; Zolotov 2012).

As mentioned above, the appearance of the set of two Raman bands (225 cm^{-1} and 275 cm^{-1}) indicates that the nanoparticulate phase formed and is found as scattered particles in the area near the decomposed pyrrhotite gains (for example, particle C and D in Fig. 8 (b)). The formation of nanoparticulate phase and the local tetrahedral disorder structure can be started by the dissolution of Fe(II) atoms from the pyrrhotite surfaces as Fe^{2+} into the aqueous solutions adjacent to the pyrrhotite surfaces.

Assuming that the major species of sulfur (S) is HS^- in aqueous solutions under moderately alkaline and reduced Eh conditions, a series of the dissolution reaction can be described as follows:

$$Fe^{3+}(aq.) + HS^- \rightarrow Fe^{2+}\ (aq.) + S\ (s) + H^+ \quad (2)$$

$$Fe_{1-x}S\ (s) + H^+ \rightarrow (1\text{-}x)\ Fe^{2+}\ (aq.) + HS^- \quad (3)$$

In these steps, locally generated H^+ by the chemical reaction (2) should play an important role for the dissolution of pyrrhotite surfaces shown as the chemical reaction (3) (Thomas et al. 1998). Further, in this reaction scheme, HS^- can be regenerated and reused in the chemical reaction (2). Elemental sulfur (S) formed by chemical reaction (2) could possibly remain on the surface. This might be responsible for the yellowish color of the pyrrhotite surface. This effective dissolution of Fe (II) atoms from the crystal lattice of pyrrhotite surface into aqueous solution is in good agreement with the experimental observation of the lower Fe/S ratio (<Fe_7S_8, $x = 0.125$) in pyrrhotite crystals in heavily aqueously altered CI chondrites (Schrader et al. 2021).

We can also observe the particles that show similar Raman bands at around 320 and 380 cm^{-1} to those of pentlandite (particles A and B in Fig. 8 (b)). These particles might be originally embedded in the pyrrhotite crystal but appeared by the dissolution of the host pyrrhotite crystal. The resistant nature of pentlandite compared to pyrrhotite during aqueous alteration of primitive meteorites was reported and discussed for CM2 and CR2 chondrites (Singerling and Brearley, 2020). The corresponding environments (pH and temperature) of the aqueous solution were implied to be pH > 6 and < 100 ℃ (Singerling and Brearley, 2020).

Aqueous solutions of alkaline pH conditions under lower temperatures were successfully modeled based on the interaction with the initial mineralogy for CI-type rocks (Zolensky et al., 1989; Rosenberg et al. 2001; Zolotov 2012). Calculations by Zolensky et al. (1989), using a solution with a starting composition of pH = 7, varied aqueous carbon concentrations (dissolved CO_2, HCO^- and CO_3^{2-}) from 10^{-8} to 10^{-2} mol / L, and anhydrous mineralogies, indicated that the gradual rise of pH, with its final value reached between 10 and 11 calculated at 50 ℃ and 99 ℃. The Mg-rich composition of the CI-type rocks accounts for alkaline pH. Such alkaline fluids dominate at low water/rock ratio (≤10), corresponding to the advanced stage of aqueous alteration (Zolotov 2012). This is also in good agreement with the estimated temperature (<90 ℃) for Ryugu particles based on O-isotope experiments (Yokoyama et al., 2023).

Fig. 9 (a) shows the appearance of the assemblage of particles found in the matrix where the pyrrhotite crystals with hexagonal morphology likely dissolved. Typical Raman spectra of these particles are shown in Fig. 9 (b) (A–D). Almost all of the particles showed Raman bands at 310 cm^{-1}, 540 cm^{-1}, and 670 cm^{-1} that were identical to magnetite ($Fe^{II}Fe_2^{III}O_4$) (de Faria et al., 1997; Shebanova and Lazor, 2003; Hanesch, 2009). These assemblages of magnetite particles are typically observed in the CI chondrites that experienced heavy aqueous alteration (Alfing et al., 2019). These features suggest that pyrrhotites are an important supplier of Fe atoms at local microenvironments for the subsequent formation of magnetite. The overall reaction can be expresses by the following scheme (Singerling and Brearley 2020).

$$3Fe_{1-x}S\ (s) + 4H_2O\ (l) \rightarrow Fe_3O_4\ (s) + 3HS^-\ (aq.) + 5H^+\ (aq.) + 2e^-\ (aq.) \quad (4)$$

In a pH vs Log fO_2 diagram, moving from the stable area of pyrrhotite to that of magnetite requires a relative increase in fO_2 (but less than that required for hematite formation) at moderately alkaline pH (Singerling and Brearley 2020). In a pH vs Eh diagram, thermodynamically stable conditions for both pyrrhotite and magnetite are located in moderately to strongly alkaline regions (pH 8 ~ 12) and strongly reducing (Eh ~ -0.5 V) conditions (Multani and Waters 2018). At the same Eh condition, moving from the stable area of pyrrhotite to that of magnetite requires a relative increase in pH from moderately (pH: 8 ~ 11) to strongly (11 ~ 12) alkaline conditions. Chemical equation (4) suggests an increase in HS^- and H^+. The presence of HS^- is in good agreement with the stable S species form for the pH and Eh conditions in aqueous solutions. The combination of H^+ and e^- may contribute the successive dissolution of Fe^{2+} from pyrrhotite surfaces by thier cathodic decomposition as shown as chemical equation (1). The H^+ may also contribute to the local increase in the acidity at the microenvironment for the dissolution of Fe(II) atoms from the pyrrhotite surfaces shown as chemical equation (3).

It is worth noting that the crystallo-chemical states recorded by Ryugu pyrrhotite surfaces measured here are in good agreement with the expected aqueous alteration conditions (alkaline pH > 6, Eh ~ -0.5 V, and low temperature < 100 ℃) modeled with thermodynamic calculations for CI's mineralogy (Zolensky et al., 1989; Rosenberg et al. 2001; Zolotov 2012), the experimental observation in low Fe/S ratio of CI pyrrhotites (Schrader et al. 2021), and experimental estimation for the alteration temperature (40℃) for Ryugu particles (Yokoyama et al., 2023). However, the intermediate chemical species between the dissolved pyrrhotite grain and the precipitated magnetite particles remain unclear and should be further investigated.

5. Conclusion

The use of N_2-gas circulation in the measurement chamber and excitation conditions that minimized heating for micro-Raman spectroscopy enabled us to measure the characteristic Raman bands centered at around 225 cm^{-1}, 275 cm^{-1}, and 313 cm^{-1} in addition to the characteristic peak for pyrrhotite at around 115 cm^{-1}. All of these bands and the peak were observed on the surfaces of pyrrhotites with both hexagonal and lath morphologies. The Raman band at around 313 cm^{-1} was assigned to the symmetric stretching motion of the local tetrahedral bonding of Fe(III)-S in $Fe^{II}_{1-3x}Fe^{III}_{1-2x}S$, where a part of the Fe(II) in the pyrrhotite lattice was changed to Fe(III), probably due to the redox reaction induced at the interface with an aqueous solution. The set of the Raman bands at around 225 cm^{-1} and 275 cm^{-1} was assigned to the typical Fe-S stretching vibrations in nanoparticulate phases and in amorphous lattice structures of iron monosulfides formed under low fO_2 condition. The corroded features with iridescence recorded on the surfaces of Ryugu pyrrotites can be explained by the dissolution of Fe atoms from the surfaces of pyrrhotites from interaction with an aqueous solution of alkaline pH and reducing Eh and under low fO_2 conditions. This is in good agreement with the low Fe/S ratio observed for CI pyrrhotites (Schrader et al. 2021) and thermodynamic calculations for aqueously altered parent bodies of carbonaceous chondrites (Zolensky et al., 1989; Rosenberg et al. 2001; Zolotov 2012). The preferential occurrence of the assemblage of magnetite $Fe^{II}Fe_2^{III}O_4$ particles was also observed in association with dissolved areas of pyrrhotites. This feature shows the importance of the local change in redox microenvironments for the dissolution and precipitation reactions via Fe^{2+}. The spectroscopic features observed here are in agreement with modeled and estimated chemical and thermodynamic conditions for aqueous alteration (alkaline pH, reducing Eh, low fO_2, and low temperature). Further spectroscopic studies on the local chemical changes of the iron sulfides and matrix minerals should bridge the chemical evolution of Fe-S-O-H_2O system and add further constraints to the alteration conditions on asteroids during the early stages of solar system formation.

Data availability

Data are available through ASTROMAT at https://doi.org/10.60520/IEDA/113276.

CRediT authorship contribution statement

Hiroharu Yui: Writing – review & editing, Writing – original draft, Supervision, Investigation, Funding acquisition, Formal analysis, Data curation, Conceptualization. **Shu-hei Urashima:** Visualization, Methodology, Investigation, Formal analysis. **Morihiko Onose:** Data curation. **Mayu Morita:** Data curation. **Shintaro Komatani:** Investigation. **Izumi Nakai:** Investigation, Funding acquisition. **Yoshinari Abe:** Investigation. **Yasuko Terada:** Investigation. **Hisashi Homma:** Investigation. **Kazuko Motomura:** Investigation. **Kiyohiro Ichida:** Investigation. **Tetsuya Yokoyama:** Investigation. **Kazuhide Nagashima:** Investigation. **Jérôme Aléon:** Investigation. **Conel M. O'D. Alexander:** Investigation. **Sachiko Amari:** Investigation. **Yuri Amelin:** Investigation. **Ken-ichi Bajo:** Investigation. **Martin Bizzarro:** Investigation. **Audrey Bouvier:** Investigation. **Richard W. Carlson:** Investigation. **Marc Chaussidon:** Investigation. **Byeon-Gak Choi:** Investigation. **Nicolas Dauphas:** Investigation. **Andrew M. Davis:** Investigation. **Wataru Fujiya:** Investigation. **Ryota Fukai:** Investigation. **Ikshu Gautam:** Investigation. **Makiko K. Haba:** Investigation. **Yuki Hibiya:** Investigation. **Hiroshi Hidaka:** Investigation. **Peter Hoppe:** Investigation. **Gary R. Huss:** Investigation. **Tsuyoshi Iizuka:** Investigation. **Trevor R. Ireland:** Investigation. **Akira Ishikawa:** Investigation.

Shoichi Itoh: Investigation. **Noriyuki Kawasaki:** Investigation. **Noriko T. Kita:** Investigation. **Kouki Kitajima:** Investigation. **Thorsten Kleine:** Investigation. **Sasha Krot:** Investigation. **Ming-Chang Liu:** Investigation. **Yuki Masuda:** Investigation. **Frédéric Moynier:** Investigation. **Ann Nguyen:** Investigation. **Larry Nittler:** Investigation. **Andreas Pack:** Investigation. **Changkun Park:** Investigation. **Laurette Piani:** Investigation. **Liping Qin:** Investigation. **Tommaso Di Rocco:** Investigation. **Sara S. Russell:** Investigation. **Naoya Sakamoto:** Investigation. **Maria Schönbächler:** Investigation. **Lauren Tafla:** Investigation. **Haolan Tang:** Investigation. **Kentaro Terada:** Investigation. **Tomohiro Usui:** Investigation. **Sohei Wada:** Investigation. **Meenakshi Wadhwa:** Investigation. **Richard J. Walker:** Investigation. **Katsuyuki Yamashita:** Investigation. **Qing-Zhu Yin:** Investigation. **Shigekazu Yoneda:** Investigation. **Edward D. Young:** Investigation. **Ai-Cheng Zhang:** Investigation. **Tomoki Nakamura:** Investigation. **Hiroshi Naraoka:** Investigation. **Takaaki Noguchi:** Investigation. **Ryuji Okazaki:** Investigation. **Kanako Sakamoto:** Investigation. **Hikaru Yabuta:** Investigation. **Masanao Abe:** Investigation. **Akiko Miyazaki:** Investigation. **Aiko Nakato:** Investigation. **Masahiro Nishimura:** Investigation. **Tatsuaki Okada:** Investigation. **Toru Yada:** Investigation. **Kasumi Yogata:** Investigation. **Satoru Nakazawa:** Investigation. **Takanao Saiki:** Investigation. **Satoshi Tanaka:** Investigation. **Fuyuto Terui:** Investigation. **Yuichi Tsuda:** Investigation. **Sei-ichiro Watanabe:** Investigation. **Makoto Yoshikawa:** Investigation. **Shogo Tachibana:** Writing – review & editing, Supervision, Project administration. **Hisayoshi Yurimoto:** Writing – review & editing, Supervision, Project administration.

Declaration of competing interest

The authors declare that they have no known competing financial interests or personal relationships that could have appeared to influence the work reported in this paper.

Acknowledgment

We would like to express our sincere appreciation to all of the scientists and engineers of the JAXA Hayabusa 2 project, whose dedication and skill brought these precious particles back to the Earth. This research was supported by Grants-in-Aid by Japan Society for the Promotion of Science (KAKENHI JP20H02773), Japan.

References

Alfing, J., Patzek, M., Bischoff, A., 2019. Modal abundances of coarse-grained (> 5 μm) components within CI-chondrites and their individual clasts – Mixing of various lithologies on the CI parent body(ies). Geochemistry 79, 125532.

Baum, A., Milosavljević, A., Lazarević, N., Radonjić, M.M., Nikolić, B., Mitschek, M., Inanloo Maranloo, Z., Šćepanović, M., Grujić-Brojčin, M., Stojilović, N., Opel, M., Wang, A., Petrovic, C., Popović, Z.V., Hackl, R., 2018. Phonon anomalies in FeS. Phys. Rev. B 97, 054306.

Berger, E.L., Zega, T.J., Keller, L.P., Lauretta, D.S., 2011. Evidence for aqueous activity on comet 81P/Wild 2 from sulfide mineral assemblages in Stardust samples and CI chondrites. Geochim. Cosmochim. Acta 75, 3501–3513.

Berger, E.L., Lauretta, D.S., Zega, T.J., Keller, L.P., 2016. Heterogeneous histories of Ni-bearing pyrrhotite and pentlandite grains in the CI chondrites Orgueil and Alais. Meteoritics Planet. Sci. 51, 1813–1829.

Boughriet, A., Figueiredo, R.S., Laureyns, J., Recourt, P., 1997. Identification of newly generated iron phases in recent anoxic sediments: ^{57}Fe Mössbauer and microRaman spectroscopic studies. J. Chem. Soc Faraday Trans. 93, 3209–3215.

Bullock, E.S., Gounelle, M., Lauretta, D.S., Grady, M.M., Russell, S.S., 2005. Mineralogy and texture of Fe-Ni sulfides in CI1 chondrites: Clues to the extent of aqueous alteration on the CI1 parent body. Geochim. Cosmochim. Acta 69, 2687–2700.

Cheng, X., Li, X., Iwasaki, I., Smith, K.A., 1998. Kinetics of cathodic decomposition of pyrrhotite and chalcopyrite in deoxygenated solutions. Miner. Metall. Process 15, 17–22.

Choi, B.-G., McKeegan, K.D., Leshin, L.A., Wasson, J.T., 1997. Origin of magnetite in oxidized CV chondrites: in situ measurement of oxygen isotope compositions of Allende magnetite and olivine. Earth Planet. Sci. Lett. 146, 337–349.

Choi, B.-G., Krot, A.N., Wasson, J.T., 2000. Oxygen isotopes in magnetite and fayalite in CV chondrites Kaba and Mokoia. Meteorit. Planet. Sci. 35, 1239–1248.

Choi, B.-G., Wasson, J.T., 2003. Microscale oxygen isotope exchange and magnetite formation in the Ningqiang anomalous carbonaceous chondrite. Geochim. Cosmochim. Acta 67, 4655–4660.

Cong, Z., Wang, M., Sun, X., Liu, L., Sun, H., 2020. Optical and dielectric properties of anodic iron oxide films. Appl. Surf. Sci. 503 (144159), 1–7.

Davidson, J., Krot, A.N., Nagashima, K., Hellebrand, E., Lauretta, D.S., 2014. Oxygen isotope and chemical compositions of magnetite and olivine in the anomalous CK3 Watson 002 and ungrouped Asuka-881595 carbonaceous chondrites: Effects of parent body metamorphism. Meteorit. Planet. Sci. 49, 1456–1474.

de Faria, D.L.A., Venâncio Silva, S., De Oliveira, M.T., 1997. Raman microspectroscopy of some iron oxides and oxyhydroxides. J. Raman Spectrosc. 28, 873–878.

El Mendili, Y., Abdelouas, A., El Hajj, H., Bardeau, J.-F., 2013. Phase transitions of iron sulphides formed by steel microbial corrosion. RSC Adv. 3, 26343.

Fujiya, W., Kawasaki, N., Nagashima, K., Sakamoto, N., Alexander, C.M.O'D., Kita, N.T., Kitajima, K., Abe, Y., Aléon, J., Amari, S., Amelin, Y., Bajo, K., Bizzarro, M., Bouvier, A., Carlson, R.W., Chaussidon, M., Choi, B.G., Dauphas, N., Davis, A.M., Di Rocco, T., Fukai, R., Gautam, I., Haba, M.K., Hibiya, Y., Hidaka, H., Homma, H., Hoppe, P., Huss, G.R., Ichida, K., Iizuka, T., Ireland, T.R., Ishikawa, A., Itoh, S., Kleine, T., Komatani, S., Krot, A.N., Liu, M.-C., Masuda, Y., McKeegan, K.D., Morita, M., Motomura, K., Moynier, F., Nakai, I., Nguyen, A., Nittler, L., Onose, M., Pack, A., Park, C., Piani, L., Qin, L., Russell, S.S., Schönbächler, M., Tafla, L., Tang, H., Terada, K., Terada, Y., Usui, T., Wada, S., Wadhwa, M., Walker, R.J., Yamashita, K., Yin, Q.-Z., Yokoyama, T., Yoneda, S., Young, E.D., Yui, H., Zhang, A.-C., Nakamura, T., Naraoka, H., Noguchi, T., Okazaki, R., Sakamoto, K., Yabuta, H., Abe, M., Miyazaki, A., Nakato, A., Nishimura, M., Okada, T., Yada, T., Yogata, K., Nakazawa, S., Saiki, T., Tanaka, S., Terui, F., Tsuda, Y., Watanabe, S., Yoshikawa, M., Tachibana, S., Yurimoto, H., 2023. Carbonate record of temporal change in oxygen fugacity and gaseous species in asteroid Ryugu. Nat. Geosci. 16, 675–682.

Genchev, G., Erbe, A., 2016. Raman Spectroscopy of Mackinawite FeS in Anodic Iron Sulfide Corrosion Products. J. Electrochem. Soc. 163, C333–C338.

Hanesch, M., 2009. Raman spectroscopy of iron oxides and (oxy)hydroxides at low laser power and possible applications in environmental magnetic studies. Geophys. J. Int. 177, 941–948.

Hansson, E.B., Odziemkowski, M.S., Gillham, R.W., 2006. Formation of poorly crystalline iron monosulfides: surface redox reactions on high purity iron, spectroelectrochemical studies. Corros. Sci. 48, 3767–3783.

Hopp, T. Dauphas, N. Abe, Y. Aléon, J., Alexander, C.M. O'D., Amari, S., Amelin, Y., Bajo, K.-I., Bizzarro, M., Bouvier, A., Carlson, R. W., Chaussidon, M., Choi, B.-G., Davis, A. M., Rocco, T.D., Fujiya, W., Fukai, R., Gautam, I., Haba, M.K., Hibiya, Y., Hidaka, H., Homma, H., Hoppe, P., Huss, G. R., Ichida, K., Iizuka, T., Ireland, T.R., Ishikawa, A., Ito, M., Itoh, S., Kawasaki, N., Kita, N. T., Kitajima, K., Kleine, T., Komatani, S., Krot, A.N., Liu, M.-C., Masuda, Y., Keegan, K.D.M., Morita, M., Motomura, K., Moynier, F., Nakai, I., Nagashima, K., Nesvorný, D., Nguyen, A., Nittler, L., Onose, M., Pack, A., Park, C., Piani, L., Qin, L., Russell, S. S., Sakamoto, N., Schönbächler, M., Tafla, L., Tang, H., Terada, K., Terada, Y., Usui, T., Wada, S., Wadhwa, M., Walker, R. J., Yamashita, K., Yin, Q.-Z., Yokoyama, T., Yoneda, S., Young, E. D., Yui, H., Zhang, A.-C., Nakamura, T., Naraoka, H., Noguchi, T., Okazaki, R., Sakamoto, K., Yabuta, H., Abe, M., Miyazaki, A., Nakato, A., Nishimura, M., Okada, T., Yada, T., Yogata, K., Nakazawa, S., Saiki, T., Tanaka, S., Terui, F., Tsuda, Y., Watanabe, S.-I., Yoshikawa, M., Tachibana, S., Yurimoto, H., 2022. Ryugu's nucleosynthetic heritage from the outskirts of the Solar System. Sci. Adv. 8, eadd8141.

Horng, C.-S., 2018. Unusual magnetic properties of sedimentary pyrrhotite in methane seepage sediments: comparison with metamorphic pyrrhotite and sedimentary greigite. J. Geophys. Res.: Solid Earth 123, 4601–4617.

Jilly-Rehak, C.E., Huss, G.R., Nagashima, K., Schrader, D.L., 2018. Low-temperature aqueous alteration on the CR chondrite parent body: Implications from *in situ* oxygen-isotope analyses. Geochim. Cosmochim. Acta 222, 230–252.

Kawasaki, N., Nagashima, K., Sakamoto, N., Matsumoto, T., Bajo, K.-I., Wada, S., Igami, Y., Miyake, A., Noguchi, T., Yamamoto, D., Russell, S. S., Abe, Y., Aléon, J., Alexander, C. M. O'D., Amari, S., Amelin, Y., Bizzarro, M., Bouvier, A., Carlson, R. W., Chaussidon, M., Choi, B.-G., Dauphas, N., Davis, A.M., Rocco, T.D., Fujiya, W., Fukai, R., Gautam, I., Haba, M.K., Hibiya, Y., Hidaka, H., Homma, H., Hoppe, P., Huss, G. R., Ichida, K., Iizuka, T., Ireland, T.R., Ishikawa, A., Ito, M., Itoh, S., Kita, N. T., Kitajima, K., Kleine, T., Komatani, S., Krot, A.N., Liu, M.-C., Masuda, Y., McKeegan, K.D., Morita, M., Motomura, K., Moynier, F., Nakai, I., Nguyen, A., Nittler, L., Onose, M., Pack, A., Park, C., Piani, L., Qin, L., Schönbächler, M., Tafla, L., Tang, H., Terad, K., Terada, Y., Usui, T., Wadhwa, M., Walker, R.J., Yamashita, K., Yin, Q.-Z., Yokoyama, T., Yoneda, S., Young, E.D., Yui, H., Zhang, A. -C., Nakamura, T., Naraoka, H., Okazaki, R., Sakamoto, K., Yabuta, H., Abe, M., Miyazaki, A., Nakato, A., Nishimura, M., Okada, T., Yada, T., Yogata, K., Nakazawa, S., Saiki, T., Tanaka, S., Terui, F., Tsuda, Y., Watanabe, S.-I., Yoshikawa, M., Tachibana, S., Yurimoto, H., 2022. Oxygen isotopes of anhydrous primary minerals show kinship between asteroid Ryugu and comet 81P/Wild2, Sci. Adv. 8, eade2067.

Lara, R.H., Monroy, M.G., Mallet, M., Dossot, M., González, M.A., Cruz, R., 2015. An experimental study of iron sulfides weathering under simulated calcareous soil conditions. Environ. Earth Sci. 73, 1849–1869.

Lin, X., Heaney, P.J., Post, J., 2018. Iridescence in metamorphic "Rainbow" hematite. Gems Gemol. 54, 28–39.

Liu, M.-C., McCain, K.A., Matsuda, N., Yamaguchi, A., Kimura, M., Tomioka, N., Ito, M., Uesugi, M., Imae, N., Shirai, N., Ohigashi, T., Greenwood, R.C., Uesugi, K., Nakato, A., Yogata, K., Yuzawa, H., Kodama, Y., Hirahara, K., Sakurai, I., Okada, I., Karouji, Y., Nakazawa, S., Okada, T., Saiki, T., Tanaka, S., Terui, F., Yoshikawa, M., Miyazaki, A., Nishimura, M., Yada, T., Abe, M., Usui, T., Watanabe, S.-I., Tsuda, Y., 2022. Incorporation of ^{16}O-rich anhydrous silicates in the protolith of highly hydrated asteroid Ryugu. Nat. Astron 6, 1172–1177.

Lutz, H.D., Müller, B., 1991. Lattice Vibration Spectra. LXVIII. single-crystal Raman spectra of marcasite-type iron chalcogenides and pnictides, FeX_2 (X = S, Se, Te; P, As, Sb). Phys. Chem. Minerals 18, 265–268.

Macdougall, J.D., Kerridge, J.F., 1977. Cubanite: A new sulfide phase in CI meteorites. Science 197, 561–562.

Martinez, L., Leinen, D., Martín, F., Gabas, M., Ramos-Barrado, J.R., Quagliata, E., Dalchieleb, E.A., 2007. Electrochemical growth of diverse iron oxide (Fe_3O_4, α-FeOOH, and γ-FeOOH) thin films by electrodeposition potential tuning. J. Electrochem. Soc. 154, D126–D133.

Matamoros-Veloza, A., Cespedes, O., Johnson, B.R.G., Stawski, T.M., Terranova, U., de Leeuw, N.H., Benning, L.G., 2018. A Highly reactive precursor in the iron sulfide system, Nature commun. 9:3125.

Mazzetti, L., Thistlethwaite, P.J., 2002. Raman spectra and thermal transformation of ferrihydrite and schwertmannite. J. Raman Spectrosc. 33, 104–111.

Mikuła, A., Dąbrowa, J., Kusior, A., Mars, K., Lach, R., Kubowicz, M., 2021. Search for mid- and high-entropy transition-metal chalcogenides – investigating the pentlandite structure. Dalton Trans. 50, 9560–9573.

Multani, R.S., Waters, K.E., 2018. A review of the physicochemical properties and floatation of pyrrhotite superstructures (4C-Fe_7S_8 / 5C-Fe_9S_{10}) in Ni-Cu sulphide mineral processing. Can. J. Chem. Eng. 96, 1185–1206.

Nakamura, T., Matsumoto, M., Amano, K., Enokido, Y., Zolensky, M.E., Mikouchi, T., Genda, H., Tanaka, S., Zolotov, M.Y., Kurosawa, K., Wakita, S., Hyodo, R., Nagano, H., Nakashima, D., Takahashi, Y., Fujioka, Y., Kikuiri, M., Kagawa, E., Matsuoka, M., Brearley, A.J., Tsuchiyama, A., Uesugi, M., Matsuno, J., Kimura, Y., Sato, M., Milliken, R.E., Tatsumi, E., Sugita, S., Hiroi, T., Kitazato, K., Brownlee, D., Joswiak, D.J., Takahashi, M., Ninomiya, K., Takahashi, T., Osawa, T., Terada, K., Brenker, F. E., Tkalcec, B.J., Vincze, L., Brunetto, R., Aléon-Toppani, A., Chan, Q.H.S., Roskosz, M., Viennet, J.-C., Beck, P., Alp, E.E., Michikami, T., Nagaashi, Y., Tsuji, T., Ino, Y., Martinez, J., Han, J., Dolocan, A., Bodnar, R. J., Tanaka, M., Yoshida, H., Sugiyama, K., King, A. J., Fukushi, K., Suga, H., Yamashita, S., Kawai, T., Inoue, K., Nakato, A., Noguchi, T., Vilas, F., Hendrix, A.R., Jaramillo-Correa, C., Domingue, D. L., Dominguez, G., Gainsforth, Z., Engrand, C., Duprat, J., Russell, S.S., Bonato, E., Ma, C., Kawamoto, T., Wada, T., Watanabe, S., Endo, R., Enju, S., Riu, L., Rubino, S., Tack, P., Takeshita, S., Takeichi, Y., Takeuchi, A., Takigawa, A., Takir, D., Tanigaki, T., Taniguchi, A., Tsukamoto, K., Yagi, T., Yamada, S., Yamamoto, K., Yamashita, Y., Yasutake, M., Uesugi, K., Umegaki, I., Chiu, I., Ishizaki, T., Okumura, S., Palomba, E., Pilorget, C., Potin, S. M., Alasli, A., Anada, S., Araki, Y., Sakatani, N., Schultz, C., Sekizawa, O., Sitzman, S. D., Sugiura, K., Sun, M., Dartois, E., Pauw, E.D., Dionnet, Z., Djouadi, Z., Falkenberg, G., Fujita, R., Fukuma, T., Gearba, I. R., Hagiya, K., Hu, M.Y., Kato, T., Kawamura, T., Kimura, M., Kubo, M.K., Langenhorst, F., Lantz, C., Lavina, B., Lindner, M., Zhao, J., Vekemans, B., Baklouti, D., Bazi, B., Borondics, F., Nagasawa, S., Nishiyama, G., Nitta, K., Mathurin, J., Matsumoto, T., Mitsukawa, I., Miura, H., Miyake, A., Miyake, Y., Yurimoto, H., Okazaki, R., Yabuta, H., Naraoka, H., Sakamoto, K., Tachibana, S., Connolly Jr., H.C., Lauretta, D.S., Yoshitake, M., Yoshikawa, M., Yoshikawa, K., Yoshihara, K., Yokota, Y., Yogata, K., Yano, H., Yamamoto, Y., Yamamoto, D., Yamada, M., Yamada, T., Yada, T., Wada, K., Usui, T., Tsukizaki, R., Terui, F., Takeuchi, H., Takei, Y., Iwamae, A., Soejima, H., Shirai, K., Shimaki, Y., Senshu, H., Sawada, H., Saiki, T., Ozaki, M., Ono, G., Okada, T., Ogawa, N., Ogawa, K., Noguchi, R., Noda, H., Nishimura, M., Namiki, N., Nakazawa, S., Morota, T., Miyazaki, A., Miura, A., Mimasu, Y., Matsumoto, K., Kumagai, K., Kouyama, T., Kikuchi, S., Kawahara, K., Kameda, S., Iwata, T., Ishihara, Y., Ishiguro, M., Ikeda, H., Hosoda, S., Honda, R., Honda, C., Hitomi, Y., Hirata, N., Hirata, N., Hayashi, T., Hayakawa, M., Hatakeda, K., Furuya, S., Fukai, R., Fujii, A., Cho, Y., Arakawa, M., Abe, M., Watanabe, S.-I., Tsuda, Y., 2023. Formation and evolution of carbonaceous asteroid asteroid Ryugu: Direct evidence from returned samples, Science 379, eabn8671.

Nakamura, E., Kobayashi, K., Tanaka, R., Kunihiro, T., Kitagawa, H., Potiszil, C., Ota, T., Sakaguchi, C., Yamanaka, M., Ratnayake, D.M., Tripathi, H., Kumar, R., Avramescu, M.-L., Tsuchida, H., Yachi, Y., Miura, H., Abe, M., Fukai, R., Furuya, S., Hatakeda, K., Hayashi, T., Hitomi, Y., Kumagai, K., Miyazaki, A., Nakato, A., Nishimura, M., Okada, T., Soejima, H., Sugita, S., Suzuki, A., Usui, T., Yada, T., Yamamoto, D., Yogata, K., Yoshitake, M., Arakawa, M., Fujii, A., Hayakawa, M., Hirata, N., Hirata, N., Honda, R., Honda, C., Hosoda, S., Iijima, Y.-I., Ikeda, H., Ishiguro, M., Ishihara, Y., Iwata, T., Kawahara, K., Kikuchi, S., Kitazato, K., Matsumoto, K., Matsuoka, M., Michikami, T., Mimasu, Y., Miura, A., Morota, T., Nakazawa, S., Namiki, N., Noda, H., Noguchi, R., Ogawa, N., Ogawa, K., Okamoto, C., Ono, G., Ozaki, M., Saiki, T., Sakatani, N., Sawada, H., Senshu, H., Shimaki, Y., Shirai, K., Takei, Y., Takeuchi, H., Tanaka, S., Tatsumi, E., Terui, F., Tsukizaki, R., Wada, K., Yamada, M., Yamada, T., Yamamoto, Y., Yano, H., Yokota, Y., Yoshihara, K., Yoshikawa, M., Yoshikawa, K., Fujimoto, M., Watanabe, S.-I., Tsuda, Y., 2022. On the origin and evolution of the asteroid Ryugu: a comprehensive geochemical perspective. Proc. Jpn. Acad. Ser. B 98, 227–282.

Nakato, A., Yada, T., Nishimura, M., Yogata, K., Miyazaki, A., Nagashima, K., Hatakeda, K., Kumagai, K., Hitomi, Y., Soejima, H., Bibring, J. –P., Pilorget, C., Hamm, V., Brunetto, R., Riu, L., Lourit, L., Loizeau, D., Le Pivert-Jolivet, T., Lequertier, G., Moussi-Soffys, A., Abe, M., Okada, T., Usui, T., Nakazawa, S., Saiki, T., Tanaka, S., Terui, F., Yoshikawa, M., Watanabe, S.-I., Tsuda, Y., 2023. Variations of the surface characteristics of Ryugu returned samples, Earth Planet. Space 75, 45.

Pankrushina, E.A., Votyakov, S.L., Aksenov, S.M., Komleva, E.V., Uporova, N.S., Vaitieva, Y.A., 2023. In situ thermo-Raman spectroscopy and ab initio vibrational assignment calculations of cubanite $CuFe_2S_3$. J. Raman Spectrosc. 54, 769–780.

Parkinson, G.S., 2016. Iron oxide surfaces. Surf. Sci. Rep. 71, 272–365.

Roberts, A.P., 2015. Magnetic mineral diagenesis. Earth Sci. Rev. 151, 1–47.

Robineau, M., Romaine, A., Sabot, R., Jeannin, M., Deydier, V., Necib, S., Refait, Ph., 2017. Galvanic corrosion of carbon steel in anoxic conditions at 80 °C associated with a heterogeneous magnetite (Fe_3O_4)/Mackinawite (FeS) layer. Electrochim. Acta 255, 274–285.

Rosenberg, N.D., Browning, L., Bourcier, W.L., 2001. Modeling aqueous alteration of CM carbonaceous chondrites. Meteorit. Planet. Sci. 36, 239–244.

Schrader, D.L., Davidson, J., McCoy, T.J., Zega, T.J., Russell, S.S., Domanik, K.J., King, A. J., 2021. The Fe/S ratio of pyrrhotite group sulfides in chondrites: An indicator of oxidation and implications for return samples from asteroids Ryugu and Bennu. Geochim. Cosmochim. Acta 303, 66–91.

Shebanova, O.N., Lazor, P., 2003. Raman spectroscopic study of magnetite ($FeFe_2O_4$): A new assignment for the vibrational spectrum. J. Solid State Chem. 174, 424–430.

Singerling, S.A., Brearley, A.J., 2020. Altered Primary iron sulfides in CM2 and CR2 carbonaceous chondrites: Insights into parent body processes.

Tachibana, S., Sawada, H., Okazaki, R., Takano, Y., Sakamoto, K., Miura, Y.N., Okamoto, C., Yano, H., Yamanouchi, S., Michel, P., Zhang, Y., Schwartz, S., Thuillet, F., Yurimoto, H., Nakamura, T., Noguchi, T., Yabuta, H., Naraoka, H., Tsuchiyama, A., Imae, N., Kurosawa, K., Nakamura, A.M., Ogawa, K., Sugita, S., Morota, T., Honda, R., Kameda, S., Tatsumi, E., Cho, Y., Yoshioka, K., Yokota, Y., Hayakawa, M., Matsuoka, M., Sakatani, N., Yamada, M., Kouyama, T., Suzuki, H., Honda, C., Yoshimitsu, T., Kubota, T., Demura, H., Yada, T., Nishimura, M., Yogata, K., Nakato, A., Yoshitake, M., Suzuki, A.I., Furuya, S., Hatakeda, K., Miyazaki, A., Kumagai, K., Okada, T., Abe, M., Usui, T., Ireland, T.R., Fujimoto, M., Yamada, T., Arakawa, M., Connolly Jr., H.C., Fujii, A., Hasegawa, S., Hirata, N., Hirose, C., Hosoda, S., Iijima, Y., Ikeda, H., Ishiguro, M., Ishihara, Y., Iwata, T., Kikuchi, S., Kitazato, K., Lauretta, D.S., Libourel, G., Marty, B., Matsumoto, K., Michikami, T., Mimasu, Y., Miura, A., Mori, O., Nakamura-Messenger, K., Namiki, N., Nguyen, A.N., Nittler, L.R., Noda, H., Noguchi, R., Ogawa, N., Ono, G., Ozaki, M., Senshu, H., Shimada, T., Shimaki, Y., Shirai, K., Soldini, S., Takahashi, T., Takei, Y., Takeuchi, H., Tsukizaki, R., Wada, K., Yamamoto, Y., Yoshikawa, K., Yumoto, K., Zolensky, M.E., Nakazawa, S., Terui, F., Tanaka, S., Saiki, T., Yoshikawa, M., Watanabe, S.-I., Tsuda, Y., 2022. Pebbles and sand on asteroid (162173) Ryugu: In situ observation and particles returned to Earth. Science 375, 1011–1016.

Tang, X., Chen, Y., 2022. A review of flotation and selective separation of pyrrhotite: a perspective from crystal structures. Int. J. Min. Sci. Technol. 32, 847–863.

Thomas, J.E., Jones, C.F., Skinner, W.M., Smart, R., St, C., 1998. The role of surface sulfur species in the inhibition of pyrrhotite dissolution in acid conditions. Geochim. Cosmochim. Acta 62, 1555–1565.

Urashima, S., Narahara, K., Yui, H., 2022. The Raman spectra of freshly cleaved pyrrhotites: the effect of atmospheric weathering and laser-induced oxidation. J. Raman Spectrosc. 53, 2179–12136.

Xi, S., Zhang, X., Luan, Z., Du, Z., Li, L., Liang, Z., Lian, C., Yan, J., 2019. Micro-Raman study of thermal transformations of sulfide and oxysalt minerals based on the heat induced by laser, Minerals 9, 751.

Xue, M., Wang, S., Wu, K., Guo, J., Guo, Q., 2011. Surface structural evolution in iron oxide thin films. Langmuir 27, 11–14.

Yokoyama, T., Nagashima, K., Nakai, I., Young, E. D., Abe, Y., Aléon, J., Alexander, C.M. O'.D., Amari, S., Amelin, Y., Bajo, K.-I., Bizzarro, M., Bouvier, A., Carlson, R. W., Chaussidon, M., Choi, B.-G., Dauphas, N., Davis, A.M., Rocco, T.D., Fujiya, W., Fukai, R., Gautam, I., Haba, M. K., Hibiya, Y., Hidaka, H., Homma, H., Hoppe, P., Huss, G. R., Ichida, K., Iizuka, T., Ireland, T. R., Ishikawa, A., Ito, M., Itoh, S., Kawasaki, N., Kita, N.T., Kitajima, K., Kleine, T., Komatani, S., Krot, A. N., Liu, M.-C., Masuda, Y., McKeegan, K. D., Morita, M., Motomura, K., Moynier, F., Nguyen, A., Nittler, L., Onose, M., Pack, A., Park, C., Piani, L., Qin, L., Russell, S. S., Sakamoto, N., Schönbächler, M., Tafla, L., Tang, H., Terada, K., Terada, Y., Usui, T., Wada, S., Wadhwa, M., Walker, R. J., Yamashita, K., Yin, Q.-Z., Yoneda, S., Yui, H., Zhang, A.-C., Connolly Jr., H. C., Lauretta, D. S., Nakamura, T., Naraoka, H., Noguchi, T., Okazaki, R., Sakamoto, K., Yabuta, H., Abe, M., Arakawa, M., Fujii, A., Hayakawa, N., Hirata, N., Hirata, R., Honda, C., Honda, S., Hosoda, Y., Iijima, I., Ikeda, H., Ishiguro, M., Ishihara, Y., Iwata, T., Kawahara, K., Kikuchi, S., Kitazato, K., Matsumoto, K., Matsuoka, M., Michikami, T., Mimasu, Y., Miura, A., Morota, T., Nakazawa, S., Namiki, N., Noda, H., Noguchi, R., Ogawa, N., Ogawa, K., Okada, T., Okamoto, C., Ono, G., Ozaki, M., Saiki, T., Sakatani, N., Sawada, H., Senshu, H., Shimaki, Y., Shirai, K., Sugita, S., Takei, Y., Takeuchi, H., Tanaka, S., Tatsumi, E., Terui, F., Tsuda, Y., Tsukizaki, R., Wada, K., Watanabe, S., Yamada, M., Yamada, T., Yamamoto, Y., Yano, H., Yokota, Y., Yoshihara, K., Yoshikawa, M., Yoshikawa, K., Furuya, S., Hatakeda, K., Hayashi, T., Hitomi, Y., Kumagai, K., Miyazaki, A., Nakato, A., Nishimura, M., Soejima, H., Suzuki, A., Yada, T., Yamamoto, D., Yogata, K., Yoshitake, M., Tachibana, S., Yurimoto, H. (2023) Samples returned from the asteroid Ryugu are similar to Ivuna-type carbonaceous meteorites. Science 379, eabn7850.

Zhou, G., Shan, Y., Wang, L., Hu, Y., Guo, J., Hu, F., Shen, J., Gu, Y., Cui, J., Liu, L., Wu, X., 2019. Photoinduced semiconductor-metal transition in ultrathin troilite FeS nanosheets to trigger efficient hydrogen evolution, Nat. Commun. 10:399.

Zolensky, M.E., Bourcier, W.L., Gooding, J.L., 1989. Aqueous alteration on the hydrous asteroids: result of EQ3/6 computer simulations. Icarus 78, 411–425.

Zolotov, M.Y., 2012. Aqueous fluid composition in CI chondritic materials: chemical equilibrium assessments in closed systems. Icarus 220, 713–729.